



Wang, S., Huang, S., Velichko, A., Wilcox, P., & Zhao, W. (2017). A multi-objective structural optimization of an omnidirectional electromagnetic acoustic transducer. *Ultrasonics*, *81*, 23-31.
<https://doi.org/10.1016/j.ultras.2017.05.014>

Peer reviewed version

License (if available):
CC BY-NC-ND

Link to published version (if available):
[10.1016/j.ultras.2017.05.014](https://doi.org/10.1016/j.ultras.2017.05.014)

[Link to publication record in Explore Bristol Research](#)
PDF-document

This is the author accepted manuscript (AAM). The final published version (version of record) is available online via Elsevier at <http://www.sciencedirect.com/science/article/pii/S0041624X17301300> . Please refer to any applicable terms of use of the publisher.

University of Bristol - Explore Bristol Research

General rights

This document is made available in accordance with publisher policies. Please cite only the published version using the reference above. Full terms of use are available:
<http://www.bristol.ac.uk/pure/about/ebr-terms>

A multi-objective structural optimization of an omnidirectional electromagnetic acoustic transducer

Shen Wang^{a,*}, Songling Huang^a, Alexander Velichko^b, Paul Wilcox^b,
Wei Zhao^a

^a*State Key Lab. of Power System, Dept. of Electrical Engineering, Tsinghua University,
Beijing 100084, China.*

^b*Dept Mech Engn, Univ Bristol, Bristol BS8 1TR, Avon, England.*

Abstract

In this paper an axisymmetric model of an omnidirectional electromagnetic acoustic transducer (EMAT) used to generate Lamb waves in conductive plates is introduced. Based on the EMAT model, the structural parameters of the permanent magnet were used as the design variables while other parameters were fixed. The goal of the optimization was to strengthen the generation of the A0 mode and suppress the generation of the S0 mode. The amplitudes of the displacement components at the observation point of the plate were used for calculation of the objective functions. Three approaches to obtain the amplitudes were discussed. The first approach was solving the peak values of the envelopes of the time waveforms from the time domain simulations. The second approach also involved calculation of the peaks, but the waveforms were from frequency domain model combined with the forward and inverse Fourier transforms. The third approach involved a single frequency in the frequency domain model. Single and multi-objective optimizations were attempted, implemented with the genetic algorithms. In the single objective optimizations, the goal was decreasing the ratio of the amplitudes of the S0 and A0 modes, while in the multi-objective optimizations, an extra goal was strengthening the A0 mode directly. The Pareto front from the multi-objective optimizations was compared with the estimation from the data on the discrete grid of the design variables. From the analysis of the results, it could be concluded that for a linearized steel plate with a thickness

*Corresponding author

Email address: wangshen@mail.tsinghua.edu.cn (Shen Wang)

of 10 mm and testing frequency of 50 kHz, the point with minimum S0/A0 could be selected, thus the multi-objective optimization effectively degenerated to the single objective optimization. While for an aluminum plate with a thickness of 3 mm and frequency of 150 kHz, without further information it would be difficult to select one particular solution from the Pareto front.

Keywords: ultrasonic transducers, omni-directional electromagnetic acoustic transducers, Lorentz force, Lamb waves, multi-objective optimization

PACS: 85.70.Ec

1. Introduction

Ultrasonic testing is widely used in various industries to check the integrity of critical structures, so as to avoid structural failure and accompanying economic losses, environmental pollutions and even human casualties. Traditionally ultrasonic waves are generated in the solid under investigation with piezoelectric transducers, but these transducers require liquid coupling to transfer the generated ultrasonic waves into the solid, and this coupling is not always convenient, and may introduce uncertainty in the testing process. As viable supplements to the piezoelectric transducers, some non-contact techniques for generating ultrasonic waves are gaining attentions these years. These non-contact techniques include air-coupled transducers, laser-generation of ultrasonic waves and electromagnetic acoustic transducers (EMATs). EMATs are the topic of this paper.

Some of the earliest analyses on EMATs and various types of ultrasonic waves they can excite could be found in Thompsons work [1, 2, 3, 4]. EMATs rely on the electromagnetic effects to generate ultrasonic waves in conductive and magnetic materials directly, without requirement for liquid coupling. In conductive solid, the EMATs work under the Lorentz force mechanism, this process is relatively simple to comprehend. While in ferromagnetic materials, besides the Lorentz forces, magnetostriction effect manifests, making the transduction process more complex [5, 6]. In this paper, we will only consider the Lorentz force in EMATs, which is a simplification if the material under testing is magnetic. Two cases will be studied in this work, i.e. a linearised steel plate and an aluminum plate. A constant magnetic permeability will be applied for the steel plate so that the magnetism is not completely ignored.

The structure of an axisymmetric EMAT is shown in Fig. 1. It's used

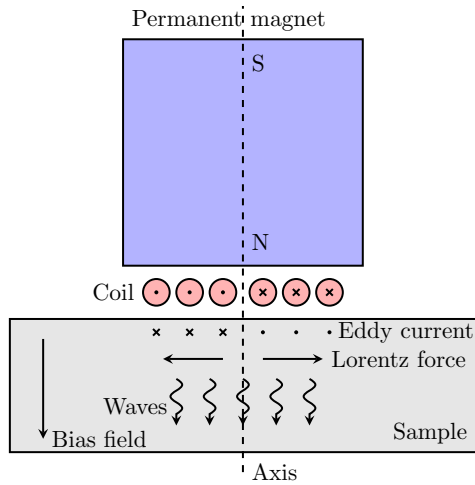


Figure 1: A typical EMAT with an axisymmetric structure. This EMAT is composed of a spiral coil and a cylindrical permanent magnet placed on a conductive solid

to generate bulk waves. The cylindrical magnet provides the vertical bias magnetic field, and the spiral coil under it is fed with alternating current. According to the electromagnetic induction law, eddy current is generated in the near surface of the tested sample. Together with the bias field, the eddy current gives rise to the Lorentz force, which then causes ultrasonic waves to propagate in the sample. This figure is only for the purpose of concept illustration, and in reality the fields can be complex. For example, the bias field provided by the magnet is not uniform in terms of magnitude and not strictly in the vertical direction. In fact, some parameters of the magnet, that determine the distribution of the bias magnetic field, are what we will use as the design variables of the optimizations.

EMATs are versatile, because with different configurations of the coil and the bias magnetic field, different kinds of ultrasonic waves could be generated. The non-contact nature of EMATs makes them suitable for some special applications like testing hot or moving objects. In spite of these obvious advantages, EMATs have their own disadvantages. One difficulty is that the energy transduction efficiency is often relatively low, and the level of magnitude of the acquired testing signal is only several microvolts. For this reason, it's always desired to build accurate models of EMATs, and design EMATs with better performance based on the models, that is, obtaining optimized parameters for these transducers.

The model of an EMAT is multiphysics in nature, involving coupling of the electromagnetic and elastodynamic fields. Modeling of EMATs has been an attractive topic in the previous years. Ludwig conducted transient analysis of a meander coil EMAT placed on isotropic non-ferromagnetic half-space, assuming uniform static magnetic field [7]. Jafari-Shapoorabadi studied in detail the controlling eddy current equations and argued that the previous work using the total current divided by the cross section area of the conductor as the source current density is equivalently applying the incomplete equation, and this means ignoring the skin effect and proximity effect [8], while we proved the opposite in [9]. Dhayalan used the FEM package COMSOL to build the electromagnetic model of a meander EMAT, and the simulated Lorentz force was exported to another package Abaqus as the driving force to excite Lamb waves [10]. These modelling work only involves non-magnetic materials. There is also some initial work on modelling EMATs used to test magnetic material, while we will not discuss further here.

The work on optimizations of EMATs are still rare. Mirkhania conducted a parametric study of an EMAT composed of a racetrack coil, by varying the ratio between the width of the magnet and the width of the coil, and found that if this ratio was set at 1.2, the ultrasonic beam amplitude would be improved [11]. One design variable and one objective function were used in this optimization, accomplished only through observation of a set of curves corresponding to different design variables instead of using a real optimization algorithm. Seher optimized a spiral coil EMAT using genetic algorithm optimization procedure in the global optimization toolbox of Matlab [12, 13]. The ratio between the amplitudes of the A0 mode and the S0 mode is selected as the objective function to be maximized, i.e. preferably generating the A0 mode. This optimization work was partly inspired by [14] in which the influence of the direction of the exciting Lorentz forces on mode selectivity was discussed with a simplified traction cone model.

In this paper, we build an axisymmetric model of an omnidirectional EMAT used to generate Lamb waves in a conductive plate, with the finite element package COMSOL. We choose COMSOL because of its power in multiphysics modelling and great flexibility. We discuss different strategies to calculate the amplitudes of displacement components at an observation point in the plate, to be used to calculate the objective functions in optimization. Then the work relating to both single objective and, more importantly, multi-objective optimizations of the EMAT is introduced, applying the genetic algorithms. The topic of multi-objective optimizations is huge

because it could be applied in so many applications in various fields including economics, finance, optimal control, process optimization, optimal design, etc. In the field of optimal design alone, diverse applications exist like nano-CMOS voltage-controlled oscillator design [15], antenna design [16], optimal sensor deployment [17], etc., while it hasn't been considered in the design of EMATs. We developed the optimization programs in Matlab, and achieved performance enhancement by decreasing the total number of evaluations of the objective functions.

In this work we followed a similar path as [12, 13], although with some distinctive differences. For the EMAT model, we chose to model each wire of the coil individually, instead of using other types of excitations, so that the waveform from frequency domain analysis and FFT/IFFT processing is close to the waveform from time-dependent analysis, because we wanted to use the latter as the reference. We divided the model into three sub-models and two geometries, so that the whole model has a clear structure. Besides the single objective optimization, we mainly focused on multi-objective optimization of the EMAT, solving the Pareto front of the problem with a MOGA program. Values of objective functions at the discrete grid of the design variables were also obtained to gain insight into the optimization problem. We developed the single objective and multi-objective genetic algorithm programs ourselves so that the performances are better compared with the code shipped with Matlab, by reducing the total number of evaluations of the objective functions, as already introduced.

2. The axisymmetric model of an omnidirectional EMAT

In this work we consider an omnidirectional EMAT composed of a spiral coil and a cylindrical permanent magnet, similar to the typical EMAT structure shown in Fig. 1. The difference is that the EMAT modelled here is used to generate Lamb waves in a plate, instead of bulk waves. One of the authors proposed an analytical model of this EMAT [18] concerning the excitability of different guided wave modes, from which the structural parameters of the coil to be used in this work are also derived from. The coil is composed of tightly wound copper wires, instead of forming a meander pattern, so both S0 mode and A0 mode Lamb waves will be generated, while in this work, the aim is to generate A0 mode Lamb waves, so we build the model bearing this preference in mind.

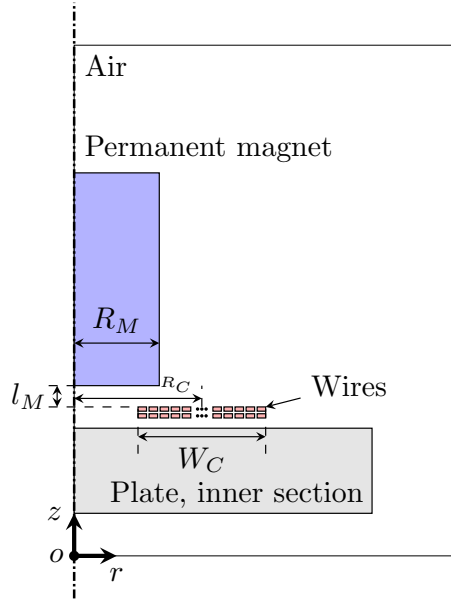


Figure 2: The geometry of the electromagnetic sub-models. This geometry is used for magnetostatic analysis and eddy current analysis.

The complete EMAT model is composed of one magnetostatic sub-model describing the magnetic field of the permanent magnet, one eddy current sub-model analysing the eddy current phenomenon accompanied by the skin and proximity effects, and one elastodynamic sub-model for simulation of wave generation and propagation in the plate. The two electromagnetic sub-models share one geometry containing the air, the inner section of the plate, the copper wires, and the permanent magnet, as in Fig. 2. Note that in this geometry only a section of the full plate is modelled. The elastodynamic sub-model has its own geometry, only containing the full plate. The Lorentz force calculated from the two electromagnetic sub-models is transferred to the elastodynamic sub-model as the driving force of ultrasonic waves. There are some benefits to use two geometries. One benefit is that the structure of the model is very clear. Another benefit is that for elastodynamic simulation, we can model the plate only, thus reducing the scale of the whole model. Additionally, we can use different meshing rules for these two geometries, according to the respective physics. This two-geometry treatment is valid because the Lorentz force is local in the region of the plate just under the transducer.

In Fig. 2, it's only necessary to consider the region where $r > 0$, since this is an axisymmetric model. The testing frequency is 50 kHz. As in [12], the relative magnetic permeability of the steel plate is 160, i.e. it's a simplified linear material. The conductivity is 4.032 MS/m (structural steel in COMSOL). The thickness of the plate is 10 mm. The remanent magnetic flux density of the magnet is set to 1.3 T (a typical value for NdFeB permanent magnet) along the positive direction of the z axis. R_M is the radius of the magnet. l_M is the liftoff distance of the magnet from its bottom to the top of the coil. The two parameters of R_M and l_M will be used as the design variables in the optimizations, while all the other parameters are fixed for each optimization.

R_C is the average radius of the coil decided as,

$$R_C = (2n - 1)\frac{\lambda}{4}, n = 1, 2, \dots \quad (1)$$

in which λ is the wavelength of the desired Lamb wave mode. For the EMAT on the steel plate, n is chosen to be 1, i.e. $R_C = \frac{\lambda}{4}$, similar as in [13]. It's not difficult to explain this equation. Because the model is axisymmetric, there is actually a cluster of wires with currents in the opposite direction in the region $r < 0$ in the actual coil (but not modeled in the axisymmetric FEM model), so a closed coil is formed. Then the distance between the centers of these two clusters of wires ($2R_C$ or the average diameter) should be half the wavelength ($2R_C = \frac{\lambda}{2}$), or we can skip this value and jump to the next proper value of R_C including another half wavelength ($R_C = \frac{\lambda}{4} + \frac{\lambda}{2}$), and so on. As stated previously, we want to selectively generate A0 mode Lamb waves. For A0 mode Lamb waves in a steel plate of 10 mm thickness at 50 kHz, from the dispersion curves generated with a program we developed, the phase velocity is 1867.78 m/s, then the wavelength λ is 37.36 mm.

W_C is the radial width of the coil (difference between the outer and inner radii of the coil). The coil is composed of two layers of copper wires with conductivity as 5.998×10^7 S/m (default value for copper material in COMSOL). The wires form an array of 23 columns and 2 rows, as in [18]. The wires have rectangular cross sections. The radial width of each wire is 0.3 mm, and the radial gap between adjacent wires in the same layer is 0.1 mm. The axial height of the wire and the gap between the two layers are both 0.1 mm. We have chosen to model each wire individually for a reason to be discussed later.

Special care must be taken when meshing the electromagnetic sub-models.

A skin layer is cut from the top surface of the plate with a thickness of 0.15 mm. In the z direction, there are 4 elements in every skin depth (8.8617×10^{-5} m for steel material) in the skin layer of the plate. The elements in the plate are rectangular elements generated with the mapped method. The remaining elements are free triangular elements. All the elements have default quadratic shape functions.

The geometry of the elastodynamic sub-model simply contains a full plate with a radius of 1.2 m. The Young's modulus is 200×10^9 Pa, Poisson's ratio is 0.33, density is 7850 kg/m^3 (structural steel). The observation point to record the displacement components in the simulations is located at 60 cm from the z axis, in the middle plane of the plate. This distance is applied to ensure that the waves are propagating stably at the observation point, as confirmed by some simulations. From the displacement wave structures of Lamb waves with the specified frequency and plate thickness, at the middle plane of the plate, the displacement component $u = u_r$ only corresponds to the S0 mode, while the other component $w = u_z$ only corresponds to the A0 mode.

In the elastodynamic sub-model, the sizes of the elements in the r direction (l_{e_r}) and the z direction (l_{e_z}) must be chosen carefully to ensure sufficient accuracy of the simulation. l_{e_z} should be small enough to make sure the number of the elements in the z direction is big enough to describe the wave structures, i.e. the distributions of the displacement, stress or any other physical variable along the thickness of the plate waveguide, accurately. 10 is adopted as the element number in the z direction for the simulation. l_{e_r} must also be small enough to ensure that there exists a sufficient number of elements in one wave length of the Lamb waves, which means that if $\lambda = C_p/f$ is the wave length and

$$\frac{\lambda}{l_{e_r}} = N \quad (2)$$

then N should be at least 10 for a good spatial resolution, and the value of 20 is recommended [19]. $N = 10$ in this work. This is reasonable considering that the default quadratic shape functions are used in discretization of the sub-model.

The boundaries of the sub-models must be handled with care. In the geometry for the electromagnetic sub-models, there is a layer of infinite elements at the air boundary simulating an air region extending to infinitely far away. This infinite element layer helps to improve the accuracy of simulation

at the air boundary. In the geometry of the elastodynamic sub-model, the top and bottom boundaries of the full plate are free boundaries without constraints or loads. For a transient analysis, the outer end edge (at $r = 1.2$ m) is also a free boundary. If the full plate is long enough in the radial direction or the total time of simulation is limited to a proper value, the reflections from the end of the plate can be avoided. While for a frequency domain analysis, an extra perfectly matched layer (PML) must be added to the end of the plate so that the energy in the plate can dissipate. In this work, the PML layer is 0.08 m in the r direction and composed of 10 layers of elements in this direction (10×10 elements in the PML region).

To further increase the accuracy of the model, fillets are added to the sharp corners of the magnet and the wires, so that the singularities are removed, while at the same time the number of elements and hence the scale of the model is also increased.

3. The time domain model vs. the frequency domain model

For optimization, we must obtain the amplitudes of the displacement components at the observation point, since they will be used to calculate the objective functions. Deciding how to calculate the amplitudes is thus crucial.

The first approach is implemented via the time-domain model. In the time-domain model, the bias magnetic field comes from the magnetostatic simulation. The eddy current distribution, and the generation and propagation of the Lamb waves are from time-dependent simulations. A time-stepping scheme is used for this simulation. For convergence of the time-dependent solver in COMSOL, a very small time step must be used, which means the simulation will be time-consuming. In this work, the number of time steps is usually set as 6000, for the tone-burst excitation signal $x(t)$ composed of 5 sinusoidal periods modulated with a Hanning window function. For a simulation time of 3.1163×10^{-4} s, the time step is 5.1938×10^{-8} s. Once the time waveforms $u(t)$ and $w(t)$ at the observation point are simulated, the amplitudes/peaks of the envelopes of these waveforms will be solved as,

$$\begin{cases} p_u &= \max(|u(t) + i\mathcal{H}[u(t)]|) \\ p_w &= \max(|w(t) + i\mathcal{H}[w(t)]|) \end{cases} \quad (3)$$

in which i is the imaginary unit, $\mathcal{H}[\cdot]$ is the Hilbert transform, $f + i\mathcal{H}[f]$ is the analytic signal corresponding to the time signal f , and the absolute value of this analytic signal gives the envelope. \max means solving the peak

of the envelope, if there's only one wave packet in the time waveform, the maximum value of the envelope corresponds to its peak. Because evolutionary algorithms will be applied in this work for optimizations, the number of evaluations of the objective function, i.e. the number of runs of the numerical model, will be big, so the time domain model is too time-consuming to be considered in optimizations, then an alternative faster approach is desired.

Another approach is to transform the input time-continuous excitation signal to its frequency components via Fourier transform (implemented with FFT on a computer), feed them into a frequency domain model, transform the output back into the time-response with inverse Fourier transform (implemented with IFFT), and finally solve the peaks of the envelopes of the time waveforms. The time waveforms obtained in this way can be expressed as,

$$\begin{cases} u(t) &= \mathcal{F}^{-1} \{ \mathcal{F}[x(t)] H_u(\omega, R_M, l_M) \} \\ w(t) &= \mathcal{F}^{-1} \{ \mathcal{F}[x(t)] H_w(\omega, R_M, l_M) \} \end{cases} \quad (4)$$

in which \mathcal{F} represents Fourier transform, \mathcal{F}^{-1} is the inverse Fourier transform, $x(t)$ is the input tone burst signal, $H_u(\omega, R_M, l_M)$ is the system function for the displacement component u along the r axis, and $H_w(\omega, R_M, l_M)$ is the system function for the displacement component w along the z axis. R_M and l_M are included to stress that these system functions change with the design variables, while the input signal $x(t)$ is fixed. Then the amplitudes/peaks are solved just like in equation (3). Because the spectrum of the input burst signal is concentrated around the center frequency, we can select only the frequency components bigger than some threshold value as an acceptable approximation. Normally tens of (or fewer) frequency components are enough, as verified by various tests, so this approach will be less time-consuming than the time-domain simulation. For this purpose, we build a frequency-domain model of the EMAT, in which the bias magnetic field is again from the magnetostatic simulation, but the eddy current sub-model and the elastodynamic sub-model are completely in the frequency-domain. Then we implement this proposed approach by connecting the frequency-domain model in COMSOL with the Matlab environment. The time waveforms from this approach are carefully compared with the waveforms from the previous time domain simulations, which serve as a reference. From many test simulations that we conducted, it was found that not every type of current or current density excitation in COMSOL could satisfy our requirement that the time waveforms from both methods be the same. For this reason, we choose to model every

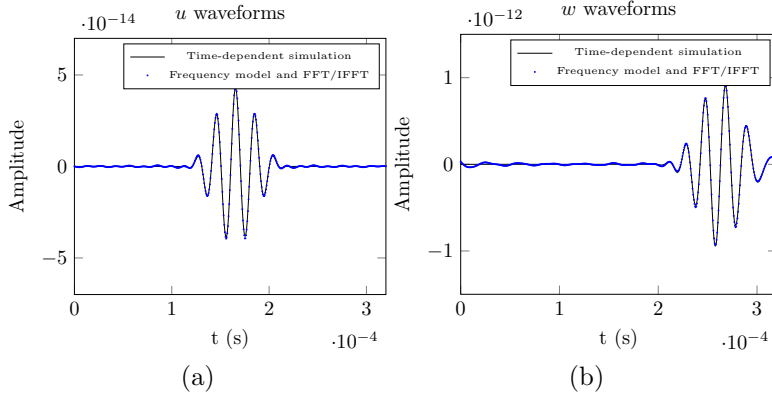


Figure 3: u and w waveforms from time-dependent simulation and frequency domain model with FFT/IFFT processing.

wire of the coil individually by specifying the total current in this wire, which is more complex than specifying other types of excitations. This is necessary because it satisfies our requirement. As an example, u and w waveforms from the time-dependent simulation and the frequency domain model with FFT/IFFT processing are compared in Fig. 3. The design variables are selected as $R_M = 8$ mm and $l_M = 1$ mm. The threshold to select the frequency components is 10%, that is, only the frequency components higher than 10% of the peak value of the spectrum are used, and others are discarded. With this threshold, 11 components around the center frequency are kept.

One important requisite to validate the frequency domain model is that the whole model must be linear. This requirement poses difficulty considering the following formulations of the Lorentz force in an EMAT,

$$\mathbf{F}_L = \mathbf{J} \times \mathbf{B} = \mathbf{J} \times (\mathbf{B}_0 + \mathbf{B}_d) \quad (5)$$

in which \mathbf{J} is the current density, \mathbf{B} is the total magnetic flux density composed of the static flux density \mathbf{B}_0 of the bias magnet, and the dynamic flux density \mathbf{B}_d generated by the excitation coil. In a frequency domain model, \mathbf{J} and \mathbf{B}_d are complex phasors, while \mathbf{B}_0 is constant, so the first part of the Lorentz force $\mathbf{J} \times \mathbf{B}_0$ is still a complex phasor, but the second part of the Lorentz force $\mathbf{J} \times \mathbf{B}_d$ is not a valid phasor, because two complex phasors cannot be multiplied to obtain another phasor. This means that the frequency model cannot handle the second part of the Lorentz force originating from the dynamic magnetic field and the current density, so we have to specify a

small value of the input current so that the Lorentz force component from the dynamic magnetic field could be ignored.

Since we are mostly concerned with the amplitudes of the u and w waveforms, yet another approach exists, where only one single-frequency is used in the frequency model. That is, we only consider the center frequency of the burst signal (50 kHz for the EMAT on the steel plate), and use the absolute values of the complex phasors to approximate the amplitudes of the waveforms. This process could be formulated as,

$$\begin{cases} |\dot{u}| &= |H_u(\omega_c, R_M, l_M)| \\ |\dot{w}| &= |H_w(\omega_c, R_M, l_M)| \end{cases} \quad (6)$$

in which ω_c is the center frequency in radian, \dot{u} is the complex phasor of u , and \dot{w} is the complex phasor of w .

It's still necessary to prove that Approach 3 is an acceptable approximation of Approach 2. By carefully observing equation (6), we can see that $|\dot{u}|$ is the system function evaluated at the center frequency. While in equation (4), the spectrum of the tone burst signal $\mathcal{F}[x(t)]$ is bell-shaped, i.e. narrow-banded, so the result of $\mathcal{F}^{-1}[\cdot]$ operation is mainly decided by the value of the system function $H_u(\omega, R_M, l_M)$ at the center frequency ω_c , if the system function is smooth (slowly changing with frequency) with respect to the spectrum of the input burst signal. Then a higher $H_u(\omega_c, R_M, l_M)$ means higher amplitude of the time waveform, and thus higher peak value of its envelope. So the phasors could be used to approximate the objective functions. Corresponding to Fig. 3, the u and w system functions are shown in Fig. 4. The spacing between two adjacent frequency components is 3.1187 kHz. These functions are indeed slowly changing with frequency compared with the spectrum of the input signal which is around 50 kHz.

The amplitudes of u , w and $\frac{u}{w}$ from Approach 2 and 3 are solved numerically with fixed $l_M = 1$ mm and different R_M values, to further validate Approach 3. The results are shown in Fig. 5. p_u is the peak value of envelope of u waveform solved with the frequency domain model and FFT/IFFT, while $|\dot{u}|$ is the magnitude of u phasor solved with one single frequency in the frequency domain model. It could be observed that the amplitudes from these two approaches are similar. In fact, the curves from the two approaches are not required to be the same. What's important is that they have similar shape and reach respective maximum values at the same set of design variables.

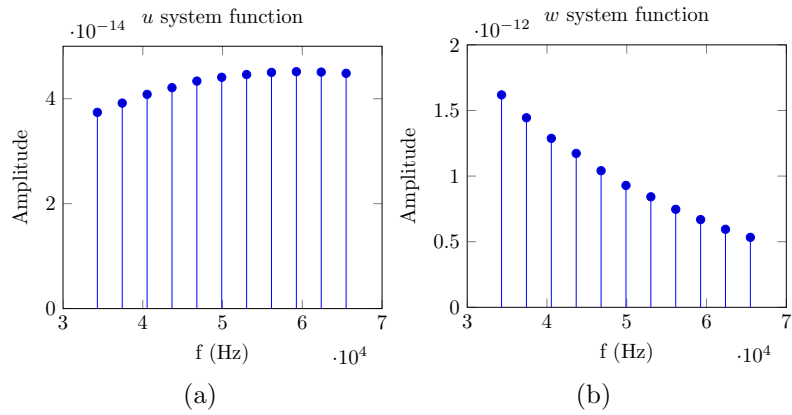


Figure 4: u and w system functions.

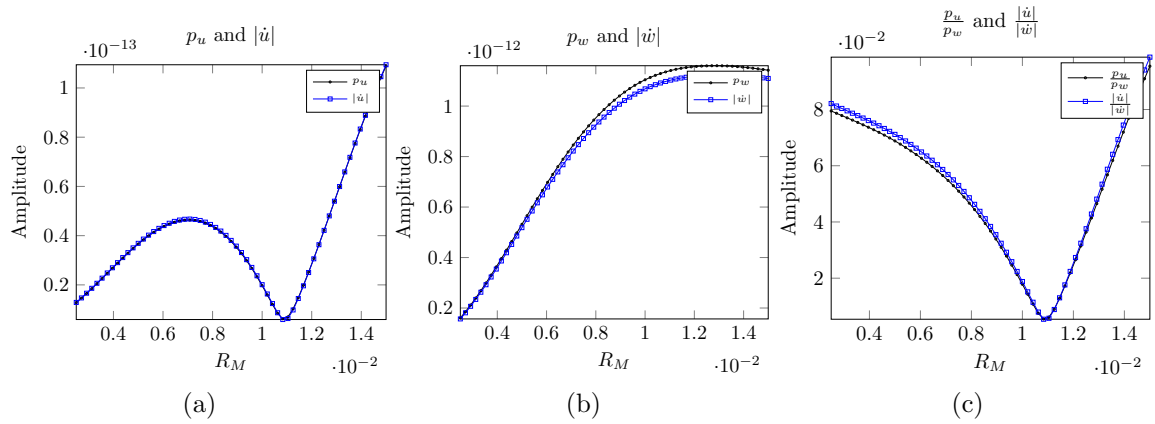


Figure 5: u , w and $\frac{u}{w}$ amplitudes at different R_M values, from Approach 2 and 3. $l_M = 1$ mm is fixed.

The third approach is the fastest, since only one frequency is used. In the later optimizations, we will mainly use this approach, although we will also compare it with the second approach, when necessary.

4. Single objective optimization of the EMAT

Firstly, we consider one objective function only. Just similar to [13], we want to selectively generate the A0 mode Lamb waves while at the same time suppress the S0 mode. So the objective function is selected as the ratio of amplitudes of the S0 mode and the A0 mode, and we need to minimize this objective function. In [13], the authors proposed to solve the displacement components at the middle plane of the plate, then from the displacement wave structures of Lamb waves, the in-plane component (u) corresponds to the S0 mode only while the out-of-plane component (w) corresponds to the A0 mode only. So the single objective optimization problem could be formulated as,

$$\text{minimize } f(R_M, l_M) = \frac{A_u}{A_w} \quad (7)$$

in which A_u is the amplitude of u and A_w is the amplitude of w . The design variables R_M and l_M have upper and lower bounds as, $R_M \in [2.5, 15]$ mm, $l_M \in [1, 3]$ mm.

For optimization, we choose the genetic algorithm (GA), a kind of global optimization algorithm without requirement to calculate gradients. We developed a genetic algorithm program in Matlab to optimize the parameters of the EMAT, i.e. the design variables. In this program, we implement binary coding and real coding, with or without constraints. The program is implemented with object-oriented programming (OOP) technique, exploiting the fact that the concepts like individual, population, generation, etc. in GA are naturally modelled with objects in OOP programming paradigm. An advantage of this program is that the total number of evaluations of the objective function is reduced, compared with the code shipped with Matlab itself. This was realized by carefully tracking the internal status of the program and avoid any unnecessary evaluations. For optimization problems involving complex numerical models, the bottleneck of the optimization procedure is the evaluation of the objective function, or running of the FEM model, so this advantage helps us reduce the total time consumed greatly.

Firstly, single frequency model is used for calculation of the objective function value in the GA program (Approach 3). The number of genera-

tions is 50, and the number of individuals is 30. Ten runs of the GA program are conducted, and the best one (with minimum value among the ten solved minimized objective function values) is that the design variables are $R_M = 10.82$ mm and $l_M = 1.14$ mm, and the corresponding objective function value is 0.00545. These results are very close to [13] where $2R_C = 21.05$ mm and $l_M = 1.47$ mm. The number of evaluations of the objective function (number of runs of the frequency domain model) is 1382, and the total time consumed is 56256 s, on a PC running Windows operating system, installed with Intel Xeon CPU @ 2.60 GHz, and a RAM of 32 GB.

Then the approach using peak values of envelopes of the time waveforms, calculated from the frequency domain model (Approach 2), is applied for comparison. The number of generations is 20, and the number of individuals is 10. Ten runs of the GA program are conducted, and the best one is that the design variables are $R_M = 10.70$ mm and $l_M = 1.19$ mm, and the corresponding objective function value is 0.00594. The number of evaluations of the objective function (number of runs of the frequency domain model with multiple frequencies and the FFT/IFFT processing) is 158, and the total time consumed is 29955 s, on the same computer. Through comparison, it could be observed that these two approaches could give similar results, so it's completely valid to use the single frequency approach in the optimizations.

5. Multi-objective optimization of the EMAT

In the previous section, only one objective function is considered, so this single objective optimization is only preliminary. In this section, two objective functions are considered simultaneously. One objective function is the ratio of the amplitudes of the S0 and A0 modes, just like in the previous section. The other objective function is the negative amplitude of the A0 mode. These two objective functions are minimized at the same time, that is, we want S0 mode to be as small as possible compared with the A0 mode, while concurrently keeping the A0 mode as big as possible. With A_u representing the amplitude of u (S0 mode) and A_w representing the amplitude of w (A0 mode), the multi-objective optimization problem is,

$$\begin{cases} \text{minimize } f_1(R_M, l_M) = \frac{A_u}{A_w} \\ \text{minimize } f_2(R_M, l_M) = -A_w \end{cases} \quad (8)$$

The concepts relating to multi-objective optimizations are more complex than those of single objective optimizations, because the multiple objective

functions are often contradictory. The concept of Pareto front is necessary, in which we generally obtain a set of optimal *non-dominated* solutions instead of a single optimal solution. A solution $\mathbf{x}^{(1)}$ (a vector of design variables) is said to *dominate* the other solution $\mathbf{x}^{(2)}$, if [20],

1. $\mathbf{x}^{(1)}$ is no worse than $\mathbf{x}^{(2)}$ in all objectives,
2. $\mathbf{x}^{(1)}$ is strictly better than $\mathbf{x}^{(2)}$ in at least one objective.

If $\mathbf{x}^{(1)}$ dominates $\mathbf{x}^{(2)}$, then $\mathbf{x}^{(2)}$ is dominated by $\mathbf{x}^{(1)}$, and $\mathbf{x}^{(1)}$ is non-dominated by $\mathbf{x}^{(2)}$. Pareto front is just a set of solutions in which any one solution is non-dominated by any other solutions in the set of all feasible solutions. Without further information, we can't say one solution on the Pareto front is better than another. For problems with two objective functions, we can draw a *criterion space* on the 2D coordinate system, in which the x axis is the value of the first objective function, and the y axis is the value of the other objective function. The Pareto front could be plotted in this criterion space.

5.1. Data on the discrete grid of the design variables

Before truly considering the problem in the point of view of multi-objective optimization, we can obtain insight of the problem by sampling the design variables R_M and l_M on a discrete grid and obtaining data including $|\dot{u}|$, $|\dot{w}|$ and $|\dot{u}|/|\dot{w}|$ on this grid. They are drawn as surfaces in Fig. 6. The two design variables are sampled on a 60×60 grid, which implies 3600 runs of the frequency domain model. Fortunately, with the approach only using one single frequency in the frequency domain model (Approach 3), the data on the grid is attainable in terms of time consumed. The $|\dot{u}|$, $|\dot{w}|$ and $|\dot{u}|/|\dot{w}|$ curves in Fig. 5 are just cut lines of these surfaces with fixed $l_M = 1$ mm.

From Fig. 6, it could be observed that the $|\dot{u}|$ surface has a special shape. The surface seems like a paper squeezed along the x axis (R_M), i.e. if we cut the surface with planes $y = l_M$ at different l_M values, the obtained curves in 3D space have similar shapes, like in Figure 5(a). On the contrary, the curves cut with planes $x = R_M$ at different R_M values are almost constant curves. This shape indicates that R_M is the dominating variable for the $|\dot{u}|$ surface, while l_M is not. The same situation exists for the $|\dot{w}|$ surface and the derived $|\dot{u}|/|\dot{w}|$ surface.

There is a valley in the $|\dot{u}|/|\dot{w}|$ surface. In this valley, the $|\dot{u}|/|\dot{w}|$ value (the original single objective function) doesn't change too much. This valley is approximately along the y axis (representing the design variable l_M), so the

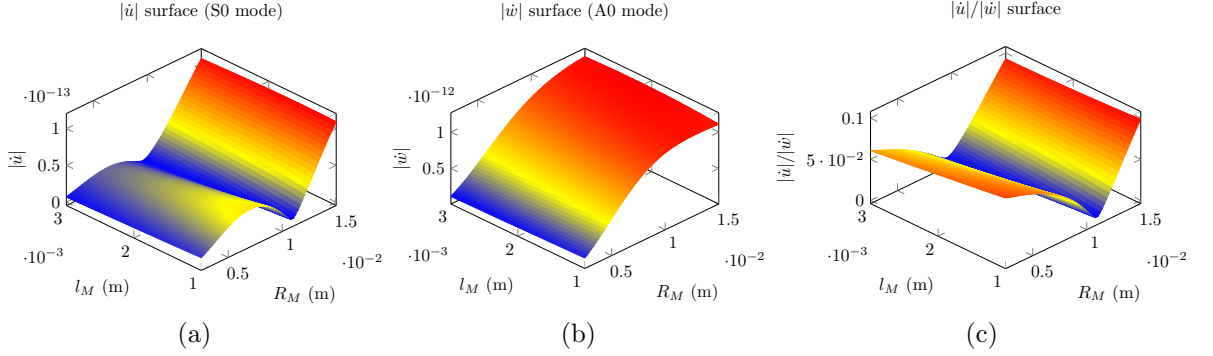


Figure 6: $|\dot{u}|$, $|\dot{w}|$ and $|\dot{u}|/|\dot{w}|$ surfaces on the discrete grid of the design variables.

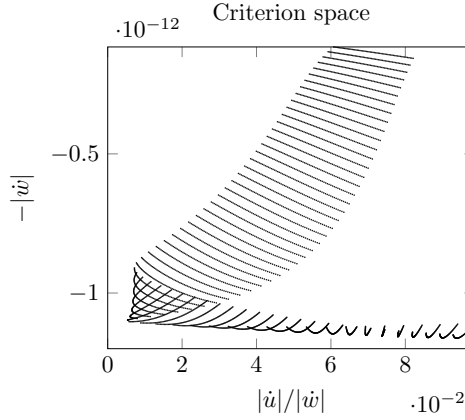


Figure 7: Scattered points corresponding to the objective function values evaluated on the discrete grid of the design variables.

$|\dot{u}|/|\dot{w}|$ value is sensitive to the variation of R_M , but not that of l_M . This is consistent with the previous observation that R_M is the dominating variable for the surfaces.

The scattered points in the criterion space corresponding to the two objective function values evaluated on the discrete grid are drawn in Fig. 7. It could be observed that the points form a smooth distribution composed of some small branches, and the shape of this distribution is also special. From this figure, we already could estimate qualitatively the Pareto front, which should be the tangent curve of the branches at the bottom of the plot, formed by closely distributed scattered points.

5.2. Optimization with the multi-objective genetic algorithm (MOGA)

Although the distribution of the scattered points can already give us an idea of what the Pareto front of the multi-objective optimization problem will look like, a dedicated optimization program is still necessary. We developed specially a multi-objective genetic algorithm program in Matlab¹ to optimize the parameters of the EMAT using two objective functions. In this program, the NSGA-II algorithm [21, 20] is implemented, and with one run of the program, the set of solutions on the Pareto front is obtained. A test case of the MOGA program is included in Appendix A. Similar to the single objective optimization program, we implemented a mechanism to track the internal status of the multi-objective optimization program, to reduce the total number of evaluations of the objective functions.

The result of one run of the multi-objective optimization is shown in Fig. 8. From the figure, the discrete solutions (marked with \times) on the Pareto front could be clearly observed. They are close to what we expect from the data on the discrete grid. If we have no further information about the problem helping us to make the decision, the Pareto front is the final result of this multi-objective optimization problem. While considering the special structure of this particular Pareto front, one possible and reasonable choice is the left most solution of the Pareto front (left most \times in Fig. 8 corresponding to $R_M = 10.84$ mm and $l_M = 1.15$ mm) where the first objective function reaches its minimum. The reason is that although the first objective function value changes greatly on this Pareto front, the second objective function doesn't change that much (from around -1.09×10^{-12} to -1.16×10^{-12}), so even if we select the solution corresponding to a minimum first objective function value, the second objective function value is not compromised too much. Note that if we select the left most solution on the Pareto front, this multi-objective optimization problem is effectively reduced to the original single-objective optimization problem.

For the optimization result corresponding to the selected solution on the Pareto front (left most solution in Fig. 8), we can feed this particular combination of the design variables ($R_M = 10.84$ mm and $l_M = 1.15$ mm) into the numerical models of the EMAT and obtain time waveforms or the pha-

¹Note that a multi-objective optimization package implemented in Matlab is desired, because it must be linked to COMSOL where the FEM model is built. COMSOL could be linked to Matlab with ease through its LiveLink feature.

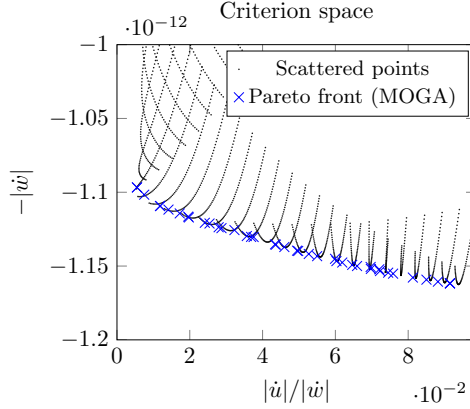


Figure 8: Pareto front solved with the MOGA. Part of the scattered points from the discrete grid of the design variables are also shown for comparison.

sors and the objective function values in the forward direction, to compare the three proposed approaches under these design variables. In Table 1, objective function values at the design variables corresponding to the selected solution on the Pareto front in the criterion space are summarized, from the three approaches. The first row is from the most time-consuming time domain simulation, and A_u and A_w are peak values of the envelopes of the S0 mode and A0 mode wave packets. The second row is also from the envelopes of the time waveforms, but the waveforms are from the frequency-domain model combined with the FFT/IFFT processing. The third row is from the least time-consuming single frequency model, which is used in the MOGA program. $|\dot{u}|$ and $|\dot{w}|$ are the absolute values of the complex phasors of the displacement components. It could be seen that with the three approaches, similar objective function values are achieved.

5.3. Optimization of an EMAT on an aluminium plate

Besides the above EMAT used for steel plate inspection (with linear simplification), an optimization is also conducted for a similar EMAT for inspection of an aluminium plate. This time the frequency is 150 kHz, and the thickness of the plate is 3 mm. The calculated phase velocity of the A0 mode is 1808.39 m/s. From a simple calculation, we can find that the resulted A0 mode wavelength is around 12 mm, then if we stick with the rule that the average radius of the coil (R_C) is $\frac{1}{4}$ of the A0 mode wavelength, i.e. $n = 1$ in equation (1), the radius will be around 3 mm, which is too small

Table 1: Objective function values at the solution selected from the Pareto front

Approaches adopted	$f_1 = A_u/A_w$	$f_2 = -A_w$ (m)
(1) Peaks of envelopes of time waveforms from time-dependent simulation, $A_u = p_u$ and $A_w = p_w$	0.005432	-1.143×10^{-12}
(2) Peaks of envelopes of time waveforms from frequency model combined with FFT/IFFT, $A_u = p_u$ and $A_w = p_w$	0.005715	-1.142×10^{-12}
(3) Absolute values of phasors from frequency-domain model with single frequency, $A_u = \dot{u} $ and $A_w = \dot{w} $ (used in the MOGA)	0.005493	-1.097×10^{-12}

for practical application. As a possible workaround, we propose to select the average radius of the coil to be $(1/4+1/2)$ wavelength of the desired A0 mode Lamb waves ($n = 2$ in equation (1)). A time-domain simulation is conducted in which the waveforms of displacement components at two different points in the plate are recorded and used to calculate the propagation velocities of the wave packets. These velocities are compared with the group velocities to validate this special design. Waveforms from frequency-domain model combined with FT/IFT also give similar results. Details are not shown here for simplicity.

Similar to the case of EMAT on a steel plate, we obtain objective function values evaluated on a discrete grid of the design variables. The bounds of the design variables are $R_M \in [0.5, 15]$ mm, $l_M \in [1, 3]$ mm. The MOGA program is also applied. The results are shown in Fig. 9. Clearly the solved Pareto front could again be estimated from the data on the discrete grid. While this time, the structure of the Pareto front is very different from that of the previous case. When the first objective function value approaches 0 (what we desire), the second objective function value also approaches 0 (what we don't want). This time, no easy decision could be made on selecting one particular solution on the Pareto front. A further investigation shows that the main reason of this difference is that with the proposed parameters of the EMAT, the $|\dot{u}|$ surface (corresponding to S0 mode) no longer has a valley

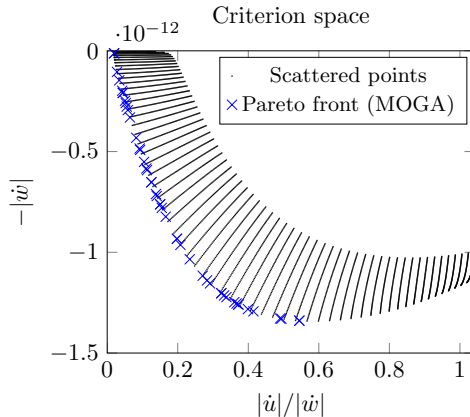


Figure 9: Pareto front solved with the MOGA, for an omnidirectional EMAT on an aluminium plate with a thickness of 3 mm at 150 kHz. The scattered points corresponding to the objective function values evaluated on the discrete grid of the design variables are also shown for comparison.

so that the derived $|\dot{u}|/|\dot{w}|$ surface doesn't have a valley, and $|\dot{w}|$ and $|\dot{u}|/|\dot{w}|$ both (almost) increase monotonically with increasing R_M at fixed l_M . The surfaces of this case are not shown here.

This situation indicates that in optimizations of EMATs, with many parameters like testing frequency, structural properties of the transducer, material properties, etc. having influences on the problem, it will be difficult to predict what the multi-objective optimization result looks like until we actually do it, unless we can build something like an analytical model to completely describe the behaviours of the transducers and the optimization procedures.

6. Conclusion

In this work we introduced an axisymmetric model of an omnidirectional EMAT composed of a spiral coil and a cylindrical magnet used to generate Lamb waves in both a steel plate (assumed to have linear magnetic property) and an aluminium plate. The model was divided into two geometries and three sub-models. This design has a clear structure, and could ensure that different physics can have different meshing rules, thus reducing the total number of elements.

The quantities we're concerned with are the amplitudes of the S0 mode and A0 mode Lamb waves, since these amplitudes are used in the opti-

mizations of the EMAT. To obtain the amplitudes, three approaches were explored. The first approach is calculating the peaks of the envelopes of the time waveforms from time-domain simulations, which is the most time-consuming. The second less time-consuming approach is also about calculating the peaks, but the time waveforms are from a frequency domain model, combined with FFT and IFFT processing. The third approach, which is the fastest, is only considering the center frequency in the frequency domain model. This approach was selected for later optimizations implemented with genetic algorithms, so as to greatly reduce the total time of optimization.

The $|\dot{u}|$, $|\dot{w}|$ and $|\dot{u}|/|\dot{w}|$ surfaces are solved for discrete grid of the design variables R_M and l_M to obtain insight of the problem. The surfaces have shapes like paper squeezed along the x axis (R_M), indicating that R_M is the dominating variable of the surfaces. For testing steel plate, the $|\dot{u}|/|\dot{w}|$ surface has a valley along the y axis (l_M), while for the EMAT on an aluminum plate, there is no valley in the $|\dot{u}|/|\dot{w}|$ surface.

A single objective genetic algorithm program and a multi-objective genetic algorithm program were developed to tackle the problem of optimizing the EMAT. Compared with the code shipped with Matlab, the number of evaluations of the objective functions is reduced. For the single objective optimization, the objective function to minimize is the ratio of amplitudes of the S0 mode and the A0 mode, meaning we want to selectively generate the A0 mode. Results from the second and third approaches are compared. For the multi-objective optimization in which the other objective function is the negative amplitude of the A0 mode, the Pareto front was obtained. This set of discrete solutions were compared with scattered points in the criterion space corresponding to the objective function values evaluated on a discrete grid of the design variables. For the case of EMAT on a steel plate, the special structure of the Pareto front allowed us to select the point corresponding to the minimum ratio of the amplitudes of the S0 and A0 modes. While for the case of EMAT on an aluminium plate, no solution on the Pareto front was more superior than the other solutions, without further information to help us make a decision. These differences in the two cases stem from the fact that for the case of steel plate, a valley exists in the $|\dot{u}|$ surface corresponding to the S0 mode Lamb waves, while there's no valley in the $|\dot{u}|$ surface for the case of EMAT on an aluminium plate.

Acknowledgment

This work was financially supported by the National Natural Science Foundation of China (grant No. 51277101 and 51107058), Tsinghua University Initiative Scientific Research Program (grant No. 20131089198), National Key Scientific Instrument and Equipment Development Project (grant No. 2013YQ140505), and China Scholarship Council (grant No. 201506215055).

The authors would like to thank the anonymous reviewers for their extensive, in-depth comments that truly improved the quality of our manuscript. We would also like to address the issue of our MOGA software availability. The software was developed for internal use only and the version available is far from being suitable to be made available to the public. To the best of our knowledge there are free packages, such as NGPM in Matlab, available that could be used to reproduce the results of this work.

Appendix A. Test case of the multi-objective GA

The KUR problem with 3 design variables and 2 objective functions was tested on the MOGA program developed.

$$\begin{cases} \text{minimize } f_1(x) = \sum_{i=1}^{n-1} \left[-10e^{-0.2\sqrt{x_i^2+x_{i+1}^2}} \right] \\ \text{minimize } f_2(x) = \sum_{i=1}^n (|x_i|^{0.8} + 5 \sin x_i^3) \end{cases} \quad (\text{A.1})$$

with $n = 3$. The lower bound vector is $[-5, -5, -5]$, and the upper bound vector is $[5, 5, 5]$. The result of the MOGA program is in Fig. A.10. The number of generations is 200, and the number of the individuals is 50. For this run, the number of evaluations of the objective functions is 9984. The Pareto front of this problem is not continuous and divided into several branches.

References

- [1] R. Thompson, Model for electromagnetic generation and detection of Rayleigh and Lamb waves, *IEEE TRANSACTIONS ON SONICS AND ULTRASONICS* SU20 (4) (1973) 340–346.
- [2] R. Thompson, Mechanisms of electromagnetic generation and detection of ultrasonic Lamb waves in iron-nickel alloy polycrystals, *JOURNAL OF APPLIED PHYSICS* 48 (12) (1977) 4942–4950.

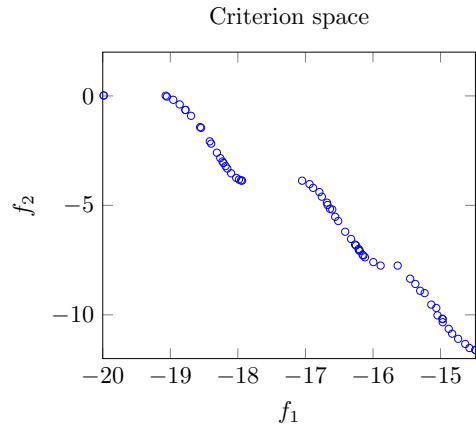


Figure A.10: Scattered points of the Pareto front of the KUR problem.

- [3] R. Thompson, Model for electromagnetic generation of ultrasonic guided waves in ferromagnetic metal polycrystals, *IEEE TRANSACTIONS ON SONICS AND ULTRASONICS* 25 (1) (1978) 7–15.
- [4] R. Thompson, Generation of horizontally polarized shear-waves in ferromagnetic materials using magnetostrictively coupled meander-coil electromagnetic transducers, *APPLIED PHYSICS LETTERS* 34 (2) (1979) 175–177.
- [5] R. Ribichini, F. Cegla, P. B. Nagy, P. Cawley, Quantitative modeling of the transduction of electromagnetic acoustic transducers operating on ferromagnetic media, *IEEE TRANSACTIONS ON ULTRASONICS FERROELECTRICS AND FREQUENCY CONTROL* 57 (12) (2010) 2808–2817.
- [6] R. Ribichini, F. Cegla, P. B. Nagy, P. Cawley, Experimental and numerical evaluation of electromagnetic acoustic transducer performance on steel materials, *NDT & E INTERNATIONAL* 45 (1) (2012) 32–38.
- [7] R. Ludwig, X. Dai, Numerical-simulation of electromagnetic acoustic transducer in the time domain, *Journal of applied physics* 69 (1) (1991) 89–98.
- [8] R. Jafari-Shapoorabadi, A. Konrad, A. Sinclair, Improved finite element method for EMAT analysis and design, *IEEE TRANSACTIONS*

- ON MAGNETICS 37 (4, 1) (2001) 2821–2823, 8th Joint Magnetism and Magnetic Materials International Magnetism Conference (MMM-INTERMAG), SAN ANTONIO, TEXAS, JAN 07-11, 2001.
- [9] S. Wang, S. Huang, Y. Zhang, W. Zhao, Multiphysics modeling of a lorentz force-based meander coil electromagnetic acoustic transducer via steady-state and transient analyses, *IEEE SENSORS JOURNAL* 16 (17) (2016) 6641–6651.
- [10] R. Dhayalan, K. Balasubramaniam, A hybrid finite element model for simulation of electromagnetic acoustic transducer (EMAT) based plate waves, *NDT & E INTERNATIONAL* 43 (6) (2010) 519–526.
- [11] K. Mirkhani, C. Chaggares, C. Masterson, M. Jastrzebski, T. Dusatko, A. Sinclair, R. Shapoorabadi, A. Konrad, M. Papini, Optimal design of EMAT transmitters, *NDT & E INTERNATIONAL* 37 (3) (2004) 181–193.
- [12] M. Seher, P. Huthwaite, M. Lowe, P. Nagy, P. Cawley, Numerical design optimization of an EMAT for A0 Lamb wave generation in steel plates, in: D. Chimenti, L. Bond, D. Thompson (Eds.), *40TH ANNUAL REVIEW OF PROGRESS IN QUANTITATIVE NONDESTRUCTIVE EVALUATION: INCORPORATING THE 10TH INTERNATIONAL CONFERENCE ON BARKHAUSEN NOISE AND MICROMAGNETIC TESTING, VOLS 33A & 33B*, Vol. 1581 of AIP Conference Proceedings, 2014, pp. 340–347.
- [13] M. Seher, P. Huthwaite, M. J. S. Lowe, P. B. Nagy, Model-based design of low frequency Lamb wave EMATs for mode selectivity, *JOURNAL OF NONDESTRUCTIVE EVALUATION* 34 (3).
- [14] P. B. Nagy, F. Simonetti, G. Instanes, Corrosion and erosion monitoring in plates and pipes using constant group velocity Lamb wave inspection, *ULTRASONICS* 54 (7) (2014) 1832–1841.
- [15] T. Ganesan, I. Elamvazuthi, P. Vasant, Multiobjective design optimization of a nano-cmos voltage-controlled oscillator using game theoretic-differential evolution, *Applied Soft Computing* 32 (2015) 293 – 299.
- [16] M. Poian, S. Poles, F. Bernasconi, E. Leroux, W. Steffe, M. Zolesi, Multi-objective optimization for antenna design, in: *2008 IEEE International*

Conference on Microwaves, Communications, Antennas and Electronic Systems, 2008, pp. 1–9.

- [17] F. Domingo-Perez, J. L. Lazaro-Galilea, A. Wieser, E. Martin-Gorostiza, D. Salido-Monzu, A. de la Llana, Sensor placement determination for range-difference positioning using evolutionary multi-objective optimization, *Expert Systems with Applications* 47 (2016) 95 – 105.
- [18] P. Wilcox, M. Lowe, P. Cawley, The excitation and detection of lamb waves with planar coil electromagnetic acoustic transducers, *IEEE TRANSACTIONS ON ULTRASONICS FERROELECTRICS AND FREQUENCY CONTROL* 52 (12) (2005) 2370–2383.
- [19] I. Bartoli, F. di Scalea, M. Fateh, E. Viola, Modeling guided wave propagation with application to the long-range defect detection in railroad tracks, *NDT & E International* 38 (5) (2005) 325–334.
- [20] K. Deb, *Multi-Objective Optimization Using Evolutionary Algorithms*, Wiley, 2001.
- [21] K. Deb, A. Pratap, S. Agarwal, T. Meyarivan, A fast and elitist multiobjective genetic algorithm: NSGA-II, *IEEE TRANSACTIONS ON EVOLUTIONARY COMPUTATION* 6 (2) (2002) 182–197.